

Framework modifications and dehydration path of a Ag⁺-modified, STI-type zeolite

Cametti, G.; Scheinost, A. C.; Giordani, M.; Churakov, S. V.;

Originally published:

May 2019

Journal of Physical Chemistry C 123(2019)22, 13651-13663

DOI: <https://doi.org/10.1021/acs.jpcc.9b01976>

Perma-Link to Publication Repository of HZDR:

<https://www.hzdr.de/publications/Publ-28951>

Release of the secondary publication
on the basis of the German Copyright Law § 38 Section 4.

Framework modifications and dehydration path of a Ag⁺-modified, STI-type zeolite

Georgia Cametti*¹, Andreas C. Scheinost^{2,3}, Matteo Giordani¹, Sergey V. Churakov^{1,4}

¹ Institute of Geological Sciences, Baltzerstrasse 1+3, 3012 Bern, Switzerland

² The Rossendorf Beamline at the European Synchrotron Radiation Facility (ESRF), Avenue des Martyrs 71, 38043 Grenoble, France

³ Institute of Resource Ecology, Bautzner Landstrasse 400, 01328 Dresden

⁴ Paul Scherrer Institut, Forschungstrasse 111, 5232 Villingen PSI, Switzerland

ABSTRACT

The effect of Ag⁺ incorporation into stellerite, a natural zeolite with **STI** framework type, was investigated by means of Single Crystal X-ray Diffraction (SC-XRD), Molecular Dynamics (MD) simulations and X-ray Absorption Fine Structure Spectroscopy (XAFS). At room temperature the complete exchange of the original extraframework ions with Ag⁺ provoked a distortion of the framework accompanied by symmetry reduction from orthorhombic *Fmmm* to monoclinic *F2/m* space group. Ag⁺ ions were strongly disordered, with occupancies ranging from 0.02 to 0.24, at partially-occupied sites within zeolitic cages. The combination of *ab initio* molecular dynamic simulations and XAFS spectroscopy suggested that Ag⁺ is coordinated by three water oxygens at 2.37 Å and by two framework oxygens at ca. 2.55 Å. The thermal stability was monitored *in situ*

by SC-XRD (from 25 to 400°C) and by XAFS (from 25 to 650°C). Upon heating the structure transformed to three different topologies: B phase, D' phase, observed here for the first time, and D phase. The unit-cell volume contracted from 4392.85(14) at room temperature to 3644.4(4) Å³, measured at 400°C. Possible Ag⁺ to Ag⁰ reduction could be excluded although the formation of Ag⁺-Ag⁺ clusters could not be unambiguously ruled out.

1. INTRODUCTION

Zeolites are microporous materials constituted by a framework of interconnected TO₄ (T mainly = Al, Si) tetrahedra^{1,2}. Each oxygen is shared by two T sites, resulting in a neutral TO₂ unit if T = Si and a negatively charged one if T = Al. The net negative charge of the framework is compensated for by extraframework cations (mainly alkaline and alkaline earth cations) which are distributed, together with H₂O, within the structural voids. The peculiar properties of zeolites such as cation exchange, selective ion sorption, and reversible dehydration, allow versatile technological applications.

Natural zeolites are abundant, low cost, and in general, have greater thermal stability and better resistance to acidic environments than many common commercial synthetic adsorbents³. On the other hand, they are variable in chemical composition and they often contain impurities. Thus, although their use in fields such as gas separation, gas purification, and catalysis, is limited compared to synthetic zeolites and other adsorbents³, natural zeolites still represent the best choice for a large variety of applications (waste-water treatment, environmental remediation^{4,5,6,7}, etc..). In addition, their low environmental impact makes them a convenient sustainable alternative. Therefore, in recent years, growing effort has been made to modify natural zeolites to tune their properties for specific tasks and to extend their range of applications^{3,8,9,10}. The modifications usually involve the substitution of their original extraframework cations (alkaline and alkaline earth

cations) with other ions (NH_4^+ , Ag^+ , Li^+ , etc.)^{11,12,13,14,15,16}. Among the possible ions, silver is of specific interest because it improves the sorption and photocatalytic properties of both synthetic and natural zeolites^{13,15,17,18,19}. Moreover, Ag-modified zeolites show high antimicrobial properties and antibacterial efficacy^{20,21}, suggesting that they can be used as more cost-effective alternative to other Ag-compounds.

Two structural aspects of Ag-modified zeolites are of paramount importance for their applications, namely i) the location of Ag^+ ions in relation to the aluminosilicate framework and the possible formation of Ag-clusters, and ii) the structural response of the Ag-modified zeolite to increase of temperature, since most of these materials are applied after thermal treatment. Although numerous studies focused on metal-exchanged zeolites^{17,18,19,20} there are only few of them dealing with natural microporous materials and in particular, there is a lack of understanding about the mechanism and the extend of structural changes as a function of temperature, which are hence in the focus of our study.

Zeolites with **STI** framework-type are medium-pore-size microporous materials with topological symmetry *Fmmm* and cell parameters $a = 13.5020$, $b = 17.8020$, $c = 17.9420$ Å, $V = 4312.6$ Å³. The framework is constituted by two systems of interconnected channels: one parallel to [001], confined by eight-membered rings (free dimensions 2.7×5.6 Å) and the other running parallel to [100], formed by ten-membered rings of tetrahedra (4.7×5.0 Å)²². The naturally occurring zeolites with **STI** framework type are quite abundant in nature: they are represented by the three endmembers stellerite²³, stilbite²⁴, and barrerite²⁵ with ideal chemical composition $\text{Ca}_8\text{Al}_{16}\text{Si}_{56}\text{O}_{144} \cdot 58\text{H}_2\text{O}$, $\text{Na}_2\text{Ca}_8\text{Al}_{18}\text{Si}_{54}\text{O}_{144} \cdot 60\text{H}_2\text{O}$, and $\text{Na}_{16}\text{Al}_{16}\text{Si}_{56}\text{O}_{144} \cdot 52\text{H}_2\text{O}$, respectively. Among synthetic phases with **STI** topology, stilbite is the most commonly used composition. It is synthesized by hydrothermal methods²⁶, and the high-silica variant, TNU-10 zeolite, is produced

in presence of 1,4-bis(N-methylpyrrolidinium)butane and Na⁺ cations as structure-directing agents²⁷.

The highest possible symmetry of **STI** framework-type materials is *Fmmm*²³. Stellerite, stilbite, and barrerite show different symmetry due to different extraframework (EF) cations and also different distribution within the zeolitic cages. Stellerite is the member with the highest symmetry *Fmmm*²³, stilbite is monoclinic *F2/m*²⁴ and barrerite is orthorhombic with space group *Amma*²⁵. The EF occupants also influence the thermal stability of the **STI** framework, as demonstrated by the different behavior upon heating of the three minerals^{28,29,30,31}. Once exchanged with the same extraframework cation, the three minerals undergo the same structural transformations driven by dehydration^{32,33}. The completely Na-exchanged forms (Na₁₆Al₁₆Si₅₆O₁₄₄ · 58H₂O) are monoclinic (space group *F2/m*) at room temperature (RT) and they are referred to as phase A^{32,33}. Upon heating T-O-T connections of the framework break leading to a different topology accompanied by unit-cell volume contraction with respect to the natural forms^{32,33}. The high temperature modification is known as phase B. Its structural topology is characterized by the statistical breaking of the T-O-T connections and the formation of a system of partially occupied face-sharing tetrahedra, mutually exclusive²⁸. Moreover, when heated *ex-situ* at 525 °C the Na-forms transform to a highly contracted (volume reduction of 19%) structure^{32,33} known as D phase³⁴. The D phase is described in the space group *A2₁ma*. The structure does not have face-sharing tetrahedra³⁴ and does not occur in natural stellerite and stilbite, which turn amorphous above 600 °C^{29,31}.

In this study we investigate the influence of Ag⁺ incorporation into a **STI** framework-type zeolite and examine the host-guest interactions as a function of temperature. In order to have a complete picture, a multi methodological approach was used. The structural data were obtained by means of Single Crystal X-ray Diffraction (SC-XRD) and the structural changes occurring upon

heating were monitored *in situ*. *Ab initio* Molecular Dynamics (MD) simulations and X-ray Absorption Fine Structure Spectroscopy (XAFS) were used to get an insight into the local structural environment of the Ag⁺ cations and to investigate the eventual formation of Ag-clusters and their oxidation state.

To the best of our knowledge this is the first time that a detailed structural investigation is performed on Ag-modified STI framework-type zeolites. We demonstrate that a new-dehydrated phase forms and that upon dehydration there is no evidence of reduction of Ag⁺. The obtained results are essential for being able to fine-tune the properties of natural zeolites and to synthesize new phases that are stable in broader conditional range (humidity and temperature) as compared to the pristine materials.

2. METHODS

The zeolite sample was a natural stellerite from Giebelsbach, Fiesch, Switzerland, with original chemical composition $\text{Ca}_{7.96}\text{K}_{0.83}\text{Na}_{0.33}(\text{Si}_{55.4}\text{Al}_{16.42})\text{O}_{144}\cdot 58.24\text{H}_2\text{O}^{35}$. In order to produce the Ag-form of stellerite (Ag-STI), natural crystals with dimensions between 0.1 and 1 mm were at first Na-exchanged (same procedure reported by Cametti et al. 2017³³). Afterwards, the Na-stellerite crystals were placed in a Teflon autoclave filled with 2M AgNO₃ solution (pH = 6) for 5 weeks at 100(2) °C. The AgNO₃ solution was renewed every three days. After the exchange process the crystals were recovered and washed with deionized water. To control successful exchange, the crystal composition was analyzed by energy dispersive spectrometry (EDS) using a scanning electron microscope (SEM).

2.1 Single Crystal X-ray Diffraction (SC-XRD). Diffraction data were collected using a Bruker APEX II single-crystal X-ray diffractometer equipped with MoK α radiation ($\lambda = 0.71073$

Å) and a CCD area detector. A crystal ($0.120 \times 0.100 \times 0.08$ mm) was glued on the tip of a glass fiber and mounted on a goniometer head. The dehydration process was investigated in step of 25°C from room temperature (RT) to 400°C by using an in-house-developed temperature controlled N_2 -blower. Each data collection lasted ca. 8 h and the equilibration time between the steps was at least 40 minutes. These experimental conditions correspond to dry conditions (relative humidity RH = 0).

Data were integrated and corrected for absorption by using the Apex 2v.2011.1-1 software package³⁶. Structure solutions were performed by Shelxtl-2008³⁷. At RT, the crystal structure of Ag-STI was solved in space group $C2/m$, transformed to $F2/m$ setting according to Quartieri et al. 1987³⁸. From 50 to 275°C the symmetry lowered from F to A centering and the structures were solved and refined in space group $A2/m$ ³³. Structure refinements were carried out using SHELXL-2014³⁹ and neutral atomic scattering factors. For structures solved in $F2/m$ and $A2/m$ the atomic coordinates and labels of framework atoms correspond to those given in Cametti et al. 2017³³. Extraframework occupants were located from difference Fourier maps. From 300 to 400°C structure solutions indicated the orthorhombic space group $A2_1ma$. The structures between 300 and 375°C did not correspond to any of the known phases of **STI** members. The atomic coordinates and labels of framework atoms of the structure obtained at 400°C were those used in Cametti et al. 2017³³. Data collected between 300 and 400°C were affected by significant smearing of the reflections, in particular in the $hk0$ plane, and decrease of reflection intensities, leading to high R_{int} and decrease of refinements quality (Table 1). Moreover, forbidden reflections in $A2/m$ (with intensities of ca. 0.6% compared to the strongest one) were detected for structures measured at 300, 325 and 350°C , indicating that in this temperature range the space group is gradually changing (see results and discussion). Additional details on structural refinements are reported as supplementary

information. Crystal data, collection and refined parameters are reported in Table 1. The drawings of the crystal structures were produced by Vesta⁴⁰. Cif files are deposited as supplementary materials.

2.2 Molecular dynamic (MD) simulations. *Ab initio* molecular dynamic simulations were used to evaluate the local hydration of extraframework cations. The simulations were performed in NPT ensemble controlling the temperature at 77°C by a stochastic canonical sampling thermostat⁴¹. The equations of motion were integrated employing 0.5 fs time step. The interatomic forces were calculated based on the density functional theory using the Gaussian and Plane Waves method (GPW) as implemented in the CP2K simulation package^{42,43}. The electron exchange and correlations were described by PBE functional⁴⁴. The Kohn–Sham orbitals were expanded using a linear combination of atom-centered Gaussian type orbital functions. In this study a “short range” double- ξ valence polarized basis set for each atomic kind was used⁴⁵. The triclinic fully flexible simulation supercell $2 \times 1 \times 1$ contained 64 extraframework cations. The data were collected from a 23 ps long MD trajectory followed by at least 6 ps pre-equilibration.

System set up. The coordinates of Na-STI³³ were taken as starting model to construct the Ag-STI structure. The *F*-centered setting of the unit cell was used to build the simulation supercell. The Al substitution for Si were randomly distributed in the framework respecting Lowenstein’s rule (Al-Al avoidance rule) resulting in the Si/Al ratio (=3.5) as obtained by chemical analysis³⁵. The Ag ions were initially placed in the crystallographic positions occupied by Na and the number of H₂O molecules was set according to the idealized chemical composition of Na-stellerite¹, i.e. $2 \times [\text{Ag}_{16}\text{Al}_{16}\text{Si}_{56}\text{O}_{144} \cdot 48\text{H}_2\text{O}]$ with 3 H₂O per Ag atom.

Theoretical EXAFS spectra were obtained using 200 consequent MD snapshots separated by 100 fs interval. EXAFS spectra for each Ag⁺ position in the supercell were calculated using FEFF 8.40

software^{46,47}. In total 32×200 spectra were averaged to obtain a reference *ab initio* EXAFS spectrum per MD trajectory. The Fermi energies and the scattering potential were calculated self-consistently using the cluster radius of 4 Å. Multi-scattering paths up to 4 legs with path lengths up to 8 Å were taken into account. Since the structural disorder is accounted for in MD trajectory the Debye-Waller factor was set to a low value of 0.006 Å². The amplitude reduction factor (S_0^2) was set to 1. A similar protocol was recently used for EXAFS spectra of structural Fe in clay minerals^{48,49}.

2.3 X-ray Absorption Fine Structure Spectroscopy (XAFS). XAFS experiments were performed at the European Synchrotron Radiation Facility (ESRF), Grenoble, France. Preliminary data were collected at the Rossendorf Beamline. The final high-temperature (HT) *in situ* measurements were performed at the Spanish CRG beamline (SPLINE, BM25) equipped with a Rh-coated collimating mirror, a sagittally focusing Si(111) double-crystal monochromator, and a Rh-coated vertically focusing mirror. The grazing angle of 2.5 mrad of both mirrors effectively suppresses the contributions of higher harmonics from the Si(111) monochromator crystal. Spectra were collected at the Ag K-edge (25514 eV) in transmission mode using gas-filled ionization chambers. A N₂ blower (FMB Oxford) was used to heat Ag-STI samples filled into a 0.7 mm capillary. The spectra were collected from 25 to 650 °C at the following temperature steps: 25, 75, 175, 275, 350, 425, 550, and 650°C. Each scan was recorded up to $k = 12 \text{ \AA}^{-1}$ with typical acquisition time of 30 min. Five scans were averaged at each temperature to improve the signal-to-noise ratio.

XAFS data reduction and Analysis. The data were reduced using the WinXas software⁵⁰. After background subtraction and normalization of the absorption edge jump to unity, the energy was converted to photoelectrons kinetic energy (k-space) by assigning the ionization energy of the Ag

K-edge to the first inflection point of the absorption edge. Pseudo radial distribution functions were obtained by Fourier transforming k^3 -weighted $\chi(k)$ functions between 2.0 and 11 \AA^{-1} using a Kaiser-Bessel window function. Structural information were extracted by a multishell fit approach using FEFF8.2^{46,47} calculated scattering paths based on the structure **used for MD simulations**. By fitting common Debye-Waller factors to the first two Ag-O and the following two Ag-Ag and Ag-Si paths, respectively, we could reduce the total number of independent fitting parameters to 11, hence remained below the Nyquist limit of 12.9 calculated for the used k-range of 2.0 to 9.5 \AA^{-1} and the used R-range of 0.9 to 3.6 \AA . The identity of the heavy Ag-Ag backscattering path was discriminated from the lighter Ag-O and Ag-Si paths by wavelet transform, employing $\sigma=1.0$ and $\varepsilon=6.0$ to maximize resolution for the Ag-Ag distance⁵¹. The amplitude reduction factor S_0^2 was fixed to 0.9 for all fits. A global phase shift ΔE_0 was fitted for all paths.

The evolution of the EXAFS spectra as a function of temperature was analyzed by Principal Component Analysis (PCA)⁵² and iterative target-transformation factor analysis (ITFA) using the software package ITFA^{53,54}. The PCA is used to identify whether a set of spectra can be represented as linear combination of a smaller number of independent components spectra, to derive the minimum number of components and finally ITFA is used to quantify the contribution of the components in each spectra⁵⁵.

Table 1 Crystal data and refinement parameters of Ag-stellerite (Ag-STI) at RT, 75 (RH = 0), 150 (RH = 0), 225 (RH = 0), 300 (RH = 0) and 400°C (RH = 0).

Crystal data	Ag-STI RT	Ag-STI 75°C	Ag-STI 150°C	Ag-STI 225°C	Ag-STI 300°C	Ag-STI 400°C
Crystal size (mm)	0.120 × 0.100 × 0.08	0.120 × 0.100 × 0.08	0.120 × 0.100 × 0.08	0.120 × 0.100 × 0.08	0.120 × 0.100 × 0.08	0.120 × 0.100 × 0.08
<i>a</i> -axis (Å)	13.6261(2)	13.6500(3)	13.6380(3)	13.5886(3)	13.5218(12)	13.0644(8)
<i>b</i> -axis (Å)	18.1650(3)	17.2956(3)	17.2793(4)	17.2521(3)	17.1991(16)	17.0283(10)
<i>c</i> -axis (Å)	17.7484(4)	16.8115(3)	16.5039(4)	16.0748(3)	16.1640(16)	16.3818(10)
β (°)	90.5490(10)	90.2300(10)	90.2150(10)	90.1630(10)	90	90
Cell volume (Å ³)	4392.85(14)	3968.91(13)	3889.20(16)	3768.43(13)	3759.1(6)	3644.4(4)
Z	1	1	1	1	1	1
Space group	<i>F</i> 2/ <i>m</i>	<i>A</i> 2/ <i>m</i>	<i>A</i> 2/ <i>m</i>	<i>A</i> 2/ <i>m</i>	<i>A</i> 2 ₁ <i>m</i>	<i>A</i> 2 ₁ <i>m</i>
Refined chemical formula	Ag _{14.5} (Si,Al) ₇₂ O ₁₄₄ ·56.3H ₂ O	Ag _{12.4} (Si,Al) ₇₂ O ₁₄₄ ·15.3H ₂ O	Ag _{12.78} (Si,Al) ₇₂ O ₁₄₄ ·5.02H ₂ O	Ag _{17.30} (Si,Al) ₇₂ O ₁₄₄	Ag _{14.57} (Si,Al) _{72.20} O ₁₄₄	Ag _{15.86} (Si,Al) ₇₂ O ₁₄₄
Data collection						
Diffraction	Bruker APEX II SMART	Bruker APEX II SMART	Bruker APEX II SMART	Bruker APEX II SMART	Bruker APEX II SMART	Bruker APEX II SMART
X-ray radiation	MoKα λ=0.71073 Å	MoKα λ=0.71073 Å	MoKα λ=0.71073 Å	MoKα λ=0.71073 Å	MoKα λ=0.71073 Å	MoKα λ=0.71073 Å
X-ray power	50 kV, 30 mA	50 kV, 30 mA	50 kV, 30 mA	50 kV, 30 mA	50 kV, 30 mA	50 kV, 30 mA
Monochromator	Graphite	Graphite	Graphite	Graphite	Graphite	Graphite
Temperature (°C)	25	75	150	225	300	400
Time per frame (s)	10	10	10	10	10	10
Max. 2θ	66.28	64.37	65.13	65.06	52.74	58.02
Index ranges	-20 < <i>h</i> < 20 -27 < <i>k</i> < 27 -27 < <i>l</i> < 25	-20 < <i>h</i> < 20 -25 < <i>k</i> < 25 -25 < <i>l</i> < 23	-20 < <i>h</i> < 20 -26 < <i>k</i> < 26 -24 < <i>l</i> < 23	-20 < <i>h</i> < 20 -26 < <i>k</i> < 26 -24 < <i>l</i> < 22	-16 < <i>h</i> < 16 -21 < <i>k</i> < 21 -19 < <i>l</i> < 20	-17 < <i>h</i> < 17 -23 < <i>k</i> < 23 -22 < <i>l</i> < 21
No. of measured reflections	31410	45948	45669	44174	27114	32128
No. of unique reflections	4313	7132	7217	6985	3695	4947
No. of observed reflections <i>I</i> > 2σ (<i>I</i>)	3561	5136	4853	4917	2652	2952
Structure refinement						
No. of parameters used in the refinement	246	437	467	464	281	213
<i>R</i> (int)	0.0393	0.0601	0.0672	0.0609	0.1322	0.1370
<i>R</i> (σ)	0.0289	0.0437	0.0510	0.0438	0.0747	0.0897
GooF	1.079	1.059	1.052	1.066	1.233	1.053
<i>R</i> 1, <i>I</i> > 2σ (<i>I</i>)	0.0620	0.0780	0.0732	0.1137	0.1162	0.1108
<i>R</i> 1, all data	0.0728	0.1034	0.1050	0.1429	0.1503	0.1607
w <i>R</i> 2 (on <i>F</i> ²)	0.1934	0.2514	0.2314	0.3214	0.3342	0.3322
Δρ _{min} (eÅ ⁻³) close to	-1.51 C2	-1.34 Ag4	-1.03 O5B	-1.64 Ag1	-0.96 O16	-1.15 T1
Δρ _{max} (eÅ ⁻³) close to	1.04 AG1E	1.52 Ag3	1.28 W1	1.18 O5B	1.29 OD1	1.24 Ag2A

3. RESULTS AND DISCUSSIONS

3.1 Structure at RT. The SEM-EDS analyses showed that Na⁺ was completely replaced by Ag⁺ (Fig. S1). The crystal structure of Ag-STI was found to be monoclinic, space group $F2/m$, $a = 13.6261(2)$, $b = 18.1650(3)$, $c = 17.7484(4)$ Å, $\beta = 90.5490(10)^\circ$, $V = 4392.85(14)$ Å³. Thus, similarly to the Na-exchanged form³³, the Ag uptake provoked a distortion of the orthorhombic symmetry. Such distortion was even more pronounced in Ag-STI as indicated by the higher value of the beta angle (90.55 and 90.06° for Ag and Na-STI³³, respectively) and by the dimension of the ten membered-ring channels (Fig. 1). These channels slightly shrink compared to that of the pristine material (Ca-STI³³).

The Ag⁺ ions at RT were strongly disordered over low-occupied sites, with occupancies ranging from 0.02 to 0.24 (Table 2). The electron density associated with EF occupants (Fig. 2a) showed that Ag⁺ ions, as well as H₂O, are spread over a large volume within the cages, making it difficult to assign precise positions to either Ag or H₂O. Several sites, close to each other, were inserted in the structural refinement to model the strong disorder (Table 2). The Ag⁺ site with highest occupancy (Ag1, occ. = 0.239(9)) was coordinated by O10 and W1 sites at the distance 2.4 - 2.5 Å. The refinement converged to R = 6.2% with the highest residual electron density peak at 1.04

Å close to Ag1E site. The estimation of the local Ag⁺ environment was based on the results from theoretical calculations and spectroscopic analysis.

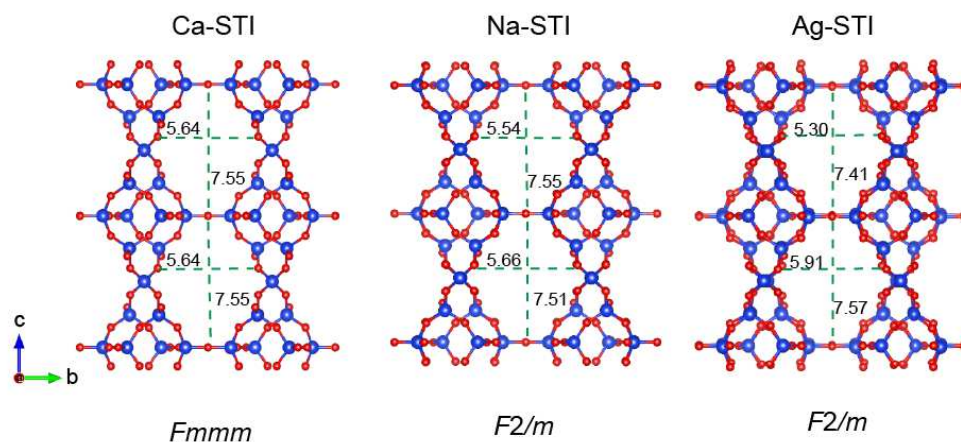


Figure 1 Ball-and-stick representation of Ca-STI³³, Na-STI³³ and Ag-STI framework projected along [100]. Space group and channels aperture (in Å) is reported for each structure.

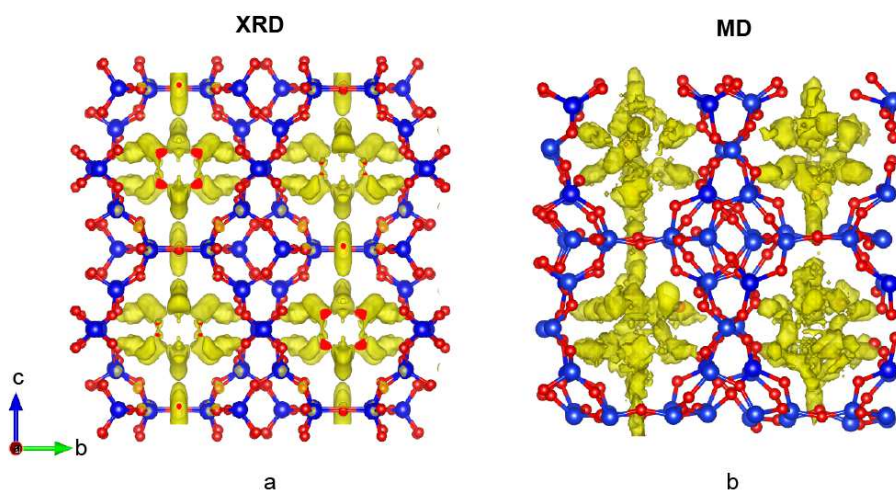


Figure 2 (a) Electron density of extraframework occupants (H₂O and Ag⁺) in Ag-STI structure obtained by SC-XRD data. Yellow isosurfaces correspond to electron density > 1.9 e⁻/Å³. For comparison the atom density distribution of O(H₂O) and Ag atoms in Ag-STI calculated by using 1400 frames in step of 10fs from MD trajectories is also shown (b).

Table 2 Atom coordinates, equivalent displacement parameters, and occupancy of Ag-STI at RT.

Site	Scattering Factor	<i>x</i>	<i>y</i>	<i>z</i>	$U^{eq}(\text{\AA}^2)$	<i>Occ.</i>
Framework						
T1	Si	0.13759(5)	-0.19277(4)	-0.12261(4)	0.01522(17)	1
T2	Si	0.13511(5)	-0.19043(4)	-0.37142(4)	0.01408(17)	1
T3	Si	-0.05081(5)	-0.41094(4)	-0.25500(4)	0.01493(17)	1
T4	Si	0.13905(5)	-0.31516(4)	-0.25075(4)	0.01379(16)	1
T5	Si	0	-0.24276(6)	-0.5	0.0163(2)	1
O1	O	0.07529(18)	-0.20382(16)	-0.04450(15)	0.0315(5)	1
O2	O	0.05984(18)	-0.18729(14)	-0.44265(15)	0.0295(5)	1
O3	O	0.1241(2)	-0.26399(16)	-0.17771(16)	0.0357(6)	1
O4	O	0.0999(2)	-0.11656(15)	-0.16443(15)	0.0341(5)	1
O5	O	0.12259(18)	-0.26858(15)	-0.32776(15)	0.0314(5)	1
O6	O	0.1135(2)	-0.12084(16)	-0.31661(16)	0.0346(6)	1
O7	O	0.24635(15)	-0.18197(15)	-0.40307(15)	0.0287(5)	1
O8	O	0.06548(16)	-0.38502(14)	-0.24935(16)	0.0296(5)	1
O9	O	-0.0536(3)	-0.5	-0.2527(3)	0.0356(8)	1
O10	O	0.25	-0.34973(19)	-0.25	0.0262(6)	1
Extraframework						
Ag1	Ag	-0.1204(10)	-0.5	-0.4176(3)	0.0494(14)	0.239(9)
Ag1A	Ag	-0.1569(13)	-0.5	-0.4007(8)	0.049(3)	0.080(5)
Ag1B	Ag	-0.212(2)	-0.5	-0.4144(19)	0.049(4)	0.022(2)
Ag1D	Ag	-0.0941(14)	-0.5	-0.4162(7)	0.008(6)	0.043(11)
Ag1E	Ag	-0.0941(16)	-0.4802(18)	-0.4312(12)	0.031(6)	0.025(5)
Ag1G	Ag	-0.199(3)	-0.5	-0.378(2)	0.049(3)	0.019(2)
Ag1F	Ag	-0.0694(19)	-0.5	-0.4180(6)	0.050(4)	0.090(10)
C1	Ag	0.1616(8)	-0.5	-0.2160(12)	0.067(3)	0.113(5)
C1A	Ag	0.1731(5)	-0.5	-0.2429(10)	0.0361(14)	0.121(4)
C1B	Ag	0.1728(6)	-0.5	-0.2682(12)	0.036(2)	0.069(5)
C1B1	Ag	0.202(3)	-0.5	-0.367(2)	0.13	0.041(3)
C1B2	Ag	0.1586(19)	-0.5	-0.303(2)	0.13	0.068(4)
C1D	Ag	0.1439(15)	-0.5	-0.1738(17)	0.067(2)	0.038(3)
C1E	Ag	0.319(2)	-0.5	-0.3713(19)	0.067(2)	0.024(2)
C2	Ag	-0.2149(8)	-0.5	-0.7503(4)	0.070(3)	0.124(5)
C3	Ag	-0.1640(12)	-0.5	-0.5469(10)	0.07	0.048(2)
C4	Ag	-0.0757(7)	-0.0894(5)	-0.4173(5)	0.137(3)	0.133(2)
C4A	Ag	-0.0253(13)	-0.0672(9)	-0.4576(11)	0.137(2)	0.077(3)
C4B	Ag	-0.0671(15)	-0.0551(11)	-0.5019(12)	0.137(2)	0.065(2)
C5	Ag	-0.1496(16)	0	-0.4518(13)	0.137(2)	0.075(3)
W1	O	-0.2844(13)	-0.5	-0.3986(8)	0.122(5)	0.90(3)
W1A	O	-0.260(4)	-0.5	-0.330(4)	0.122(14)	0.20(2)

W2	O	-0.3416(11)	-0.5	-0.3833(7)	0.033(3)	0.49(4)
W2A	O	-0.3715(12)	-0.5	-0.4012(7)	0.033(4)	0.52(5)
W3	O	-0.269(2)	-0.1220(9)	-0.4429(9)	0.076(7)	0.40(5)
W3A	O	-0.222(2)	-0.1211(9)	-0.4446(9)	0.099(7)	0.48(5)
W3B	O	-0.2573(13)	-0.1716(11)	-0.4600(10)	0.057(6)	0.236(18)
W6	O	-0.0391(13)	-0.5705(14)	-0.5377(14)	0.15	0.58(3)
W6A	O	-0.0785(13)	-0.6079(8)	-0.5737(8)	0.054(4)	0.34(2)
W6B	O	-0.0458(14)	-0.5911(10)	-0.5596(10)	0.029(8)	0.18(3)
W7	O	-0.4111(18)	-0.5	-0.4142(10)	0.074(5)	0.55(4)

3.1.2. Local environment of Ag⁺ ions. A snapshot of the Ag-STI structure obtained by MD simulations is reported in Fig. 2b. The distribution density of Ag⁺ and H₂O-oxygen within the channels averaging 1400 frames in steps of 10fs from MD trajectories, shows that Ag⁺ and H₂O positions dynamically change within the cage even on the short time scale of MD simulations. Apparent cage to cage variation of Ag⁺ and H₂O distributions is the consequence of the limited sampling time. Using the supercell, the averaged pattern of Ag⁺ and H₂O distribution in the cage is in good agreement with X-ray data. The calculated unit-cell parameters (Table 3) were close to those determined by X-ray diffraction with deviation of 0.2, 1.08, and 0.07 % for a, b, and c length respectively and 3% for the beta angle. The average <Ag-O> distance to the H₂O molecules (O_w) was found to be 2.35 Å. In contrast, framework (O) oxygen atoms were broadly distributed at distances between 2.55 and 3.00 Å as indicated by the radial distribution function shown in Fig. 3a. The running coordination number RNC(*d*) (i.e. how many atoms surround an Ag⁺ at a given distance *r*(Å)) calculated for the Ag-O, Ag-O_w, Ag-Si, and Ag-Al interactions is also reported in Fig.3. On average (Fig. 3a) Ag⁺ is coordinated by three H₂O and by two framework oxygen at bonding distances between 2.35-3.00 Å, and 2.55–3.10 Å, respectively.

The $k^3\chi(k)$ weighted-EXAFS and the corresponding Fourier Transform (FT) best fits of the sample measured at 25°C are reported in Fig. 4. In agreement with theoretical computations and SC-XRD

data, the FT (uncorrected for the phase shift) indicates the lack of long-range order of Ag atoms within the zeolite structure.

The best fit was obtained by using four shells, two Ag-O for a split coordination environment, one Ag-Ag, and one Ag-Si shell (Table 4). The first peak of the Fourier transform magnitude (FTM) at ca. 1.80 Å (FTM distance uncorrected for phase shift) can be attributed to the Ag-O shells, fitted with a split-oxygen model: 3.2 oxygen at 2.37 Å and 1.1 at 2.14 Å from Ag. Beyond this peak and up to about 3.5 Å, the FTM shows a much smaller double peak. The wavelet plot employing a Morlet wavelet reveals not only the Ag-O backscattering peak with a maximum at about $k = 4 \text{ \AA}^{-1}$, but also a tail at about 9 \AA^{-1} , which becomes more clearly pronounced with higher temperature (Fig. S2). This peak indicates the presence of a backscatterer with much higher electron density, which in this chemically confined system can only be a Ag-Ag backscattering path. Fitting this path alone, however, was not sufficient to fit the FTM and imaginary parts of this R-region; only after introduction of an Ag-Si path the fit improved significantly (note that the similar electron density of Si and Al backscatterers does not allow to distinguish them). The fit parameters show about 0.3 Si atoms at a distance of 3.76 Å and about 0.2 Ag atoms at 2.92 Å. The 3.2 O atoms at 2.37 Å are in excellent agreement with the three water molecules at this distance derived by MD simulations. The distance of the Si atom is also in good agreement with the result from MD (3.7 Å); the low coordination number of 0.2 is certainly due to the fact, that only a smaller fraction of Ag atoms is in a well-defined orientation towards the zeolite framework structure. Ag-Ag backscattering paths at 2.92 Å with low coordination number suggest that few Ag-Ag pairs are forced into proximity within the zeolite cages; although this distance is close to the 2.89 Å expected for elemental Ag, the XANES spectra (Fig. S3) show only monovalent Ag.

Table 3 Unit-cell parameters of Ag-STI obtained from MD trajectories and SC-XRD data collected at RT. The deviation (in percentage) of MD unit-cell parameters from those obtained by SC-XRD is shown.

	MD	XRD	Deviation
a -axis (Å)	13.6027	13.6261(2)	0.2%
b -axis (Å)	17.96874	18.1650(3)	1.08%
c -axis (Å)	17.73644	17.7484(4)	0.07%
α (°)	89.95	90	0.06%
β (°)	87.678	90.5490(10)	3.1%
γ (°)	89.76	90	0.27%
Cell volume (Å ³)	4334.15	4392.85(14)	1.3%

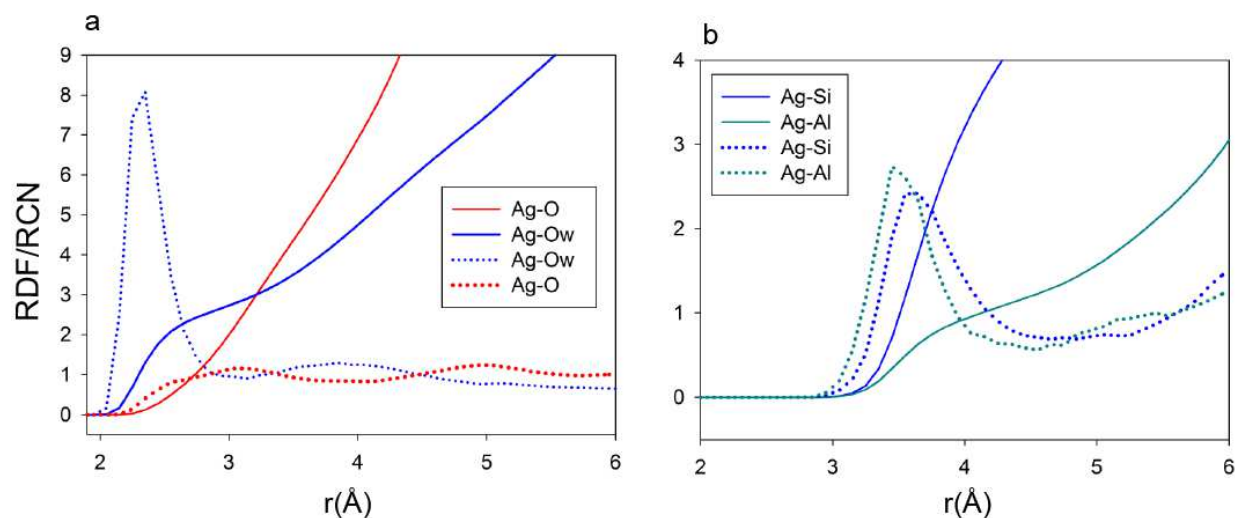


Figure 3 Radial Distribution Function (RDF) and Running Coordination Number (RCN) of (a) Ag-O (oxygen belonging to the framework) and Ag-Ow (oxygen of H₂O) and (b) of Ag-Si and Ag-Al obtained from MD trajectories. Dotted and continuous lines indicate RDF and RCN, respectively.

Table 4 Structural parameters of Ag-STI at 25 and 650°C determined from EXAFS data. The uncertainty for each parameter is also reported.

Shell	25°C			650°C		
	CN ±25%	R(Å) ±0.01	σ^2 (Å ²) ±0.002	CN±25%	R(Å) ±0.01	σ^2 (Å ²) ±0.002
Ag-O	3.2	2.37	0.0136*	1.5	2.33	0.0019*
Ag-O	1.1	2.14	0.0136*	1.4	2.10	0.0019*
Ag-Si	0.3	3.76	0.0041*	1.0	3.44	0.0181*
Ag-Ag	0.2	2.92	0.0041*	1.9	3.31	0.0181*
ΔE_0		1.2			-5.3	
χ -residual		5.2			4.9	

*constrained to be equal

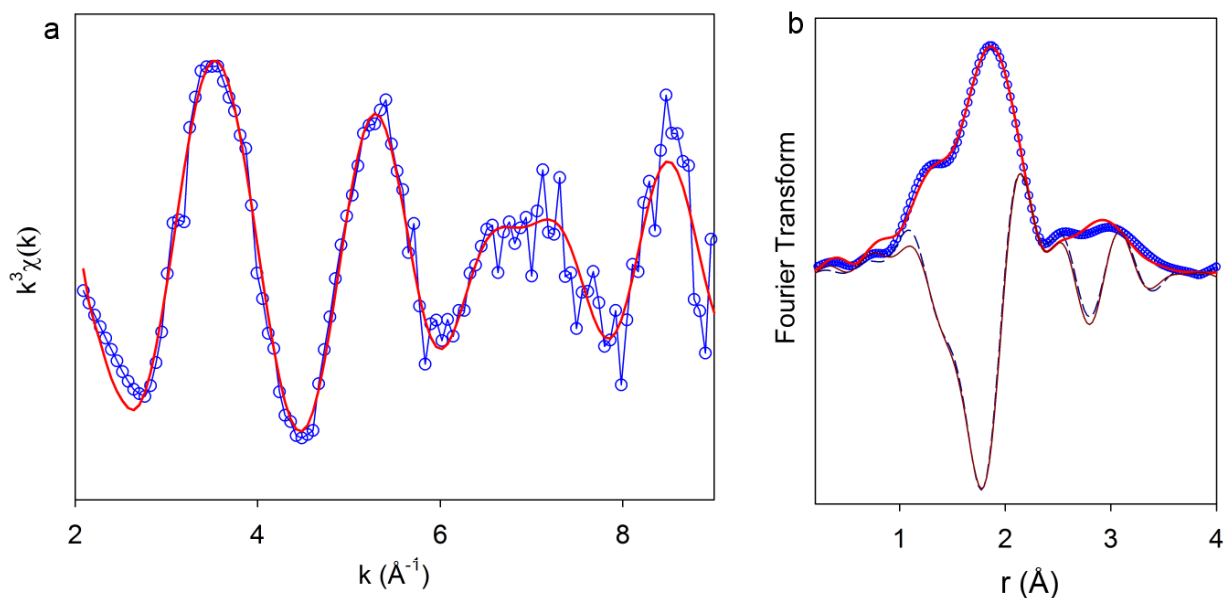


Figure 4 (a) $k^3\chi(k)$ weighted and (b) Fourier-transformed EXAFS spectra (uncorrected shift) of Ag-STI at 25°C. Experimental data and corresponding fit are shown as blue circles and red line, respectively. Measured (dashed line) and fitted (continuous line) imaginary parts of FT are also displayed.

Note also that this EXAFS-derived Ag-Ag distance is slightly shorter than that predicted by MD simulations ($> 3.16 \text{ \AA}$). Although the Ag-Ow, Ag-Ag and Ag-Si shells derived from EXAFS agree quite well with the MD simulations, there are also important differences: First, EXAFS shows an additional Ag-O distance of 2.14 \AA , which is absent in the MD simulations. Such a short distance occurs in the room-temperature, low-pressure structure of Ag_2O^{56} , where Ag is bound by 3 O atoms at 2.16 \AA , and furthermore coordinated to 6 Ag atoms at 3.04 \AA and 6 more Ag atoms at 3.07 \AA . Ag_2O has a fairly low solubility in water and hence may have formed during the cation exchange. **This assumption was confirmed by the occurrence of small Ag-rich particles in the powder used for EXAFS measurements** (Fig. S4). Second, MD simulations showed the

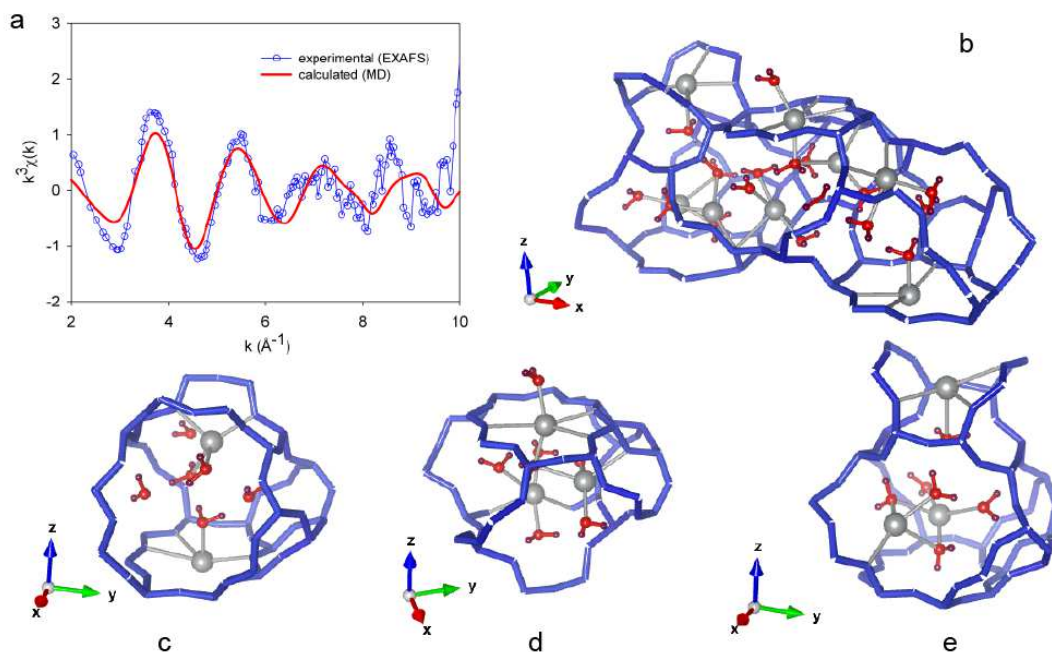


Figure 5 (a) Experimental (blue circles) and calculated (red line) k^3 -weighted $\chi(k)$ function obtained from EXAFS and MD simulations. (b) Snapshot from MD simulations showing the positions of Ag ions within adjacent cages in Ag-STI structure; (c,d,e) detail of a single cage and corresponding Ag^+ coordination. Ag^+ ions are shown as grey spheres; H_2O are shown as red (O) and dark purple (H) spheres; the framework is represented by blue sticks obtained by T-O-T connections; Ag-O bonds are displayed as grey cylinders.

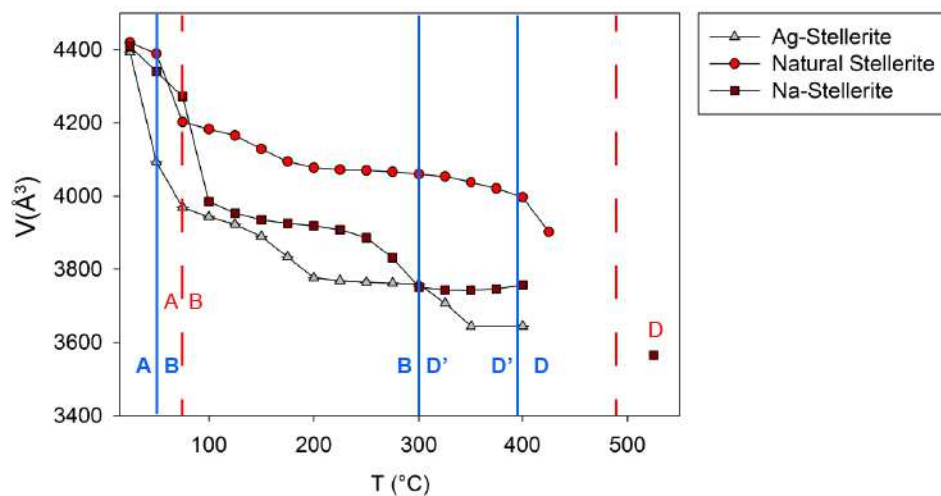


Figure 6 Unit-cell volume contraction of Ag-STI (grey triangles) as a function of temperature. Unit-cell volume of Ca-STI (red circles) and Na-STI (dark-red squares)³³ are also reported for comparison. The vertical continuous lines indicate the A-B, B-D', and D'-D transitions of Ag-STI. The dashed lines refer to A-B and B-D transitions in Na-STI³³.

coordination of Ag to O atoms of the framework between 2.55 and 3.0 Å, which could not be determined by EXAFS shell fit, most probably because of their high disorder. Given these discrepancies between the MD-derived and the EXAFS-derived local structures, the limited match between the ab initio EXAFS spectrum calculated from MD trajectories and the experimental spectrum is not surprising (Fig. 5a).

A representative snapshot from MD simulations in Fig. 5b, shows instantaneous positions of Ag ions in adjacent cages. Ag⁺ ions can be typically found at the bottom of the t-sti-1* cage (nomenclature according to Smith, 1988⁵⁷) in the center of the 8-membered ring window (Fig. 5c) where they mainly bond to framework oxygen and one H₂O. Alternatively, Ag⁺ ions are located in the middle of the cage (Fig. 5 d,e) where they are mainly surrounded by H₂O.

3.2 Structural modifications upon heating. Due to strong disorder of the EF occupants and the difficulty to assess H₂O positions, the release of water and, as a consequence, the exact amount of H₂O retained by the Ag-STI at each temperature could not be unambiguously determined. The

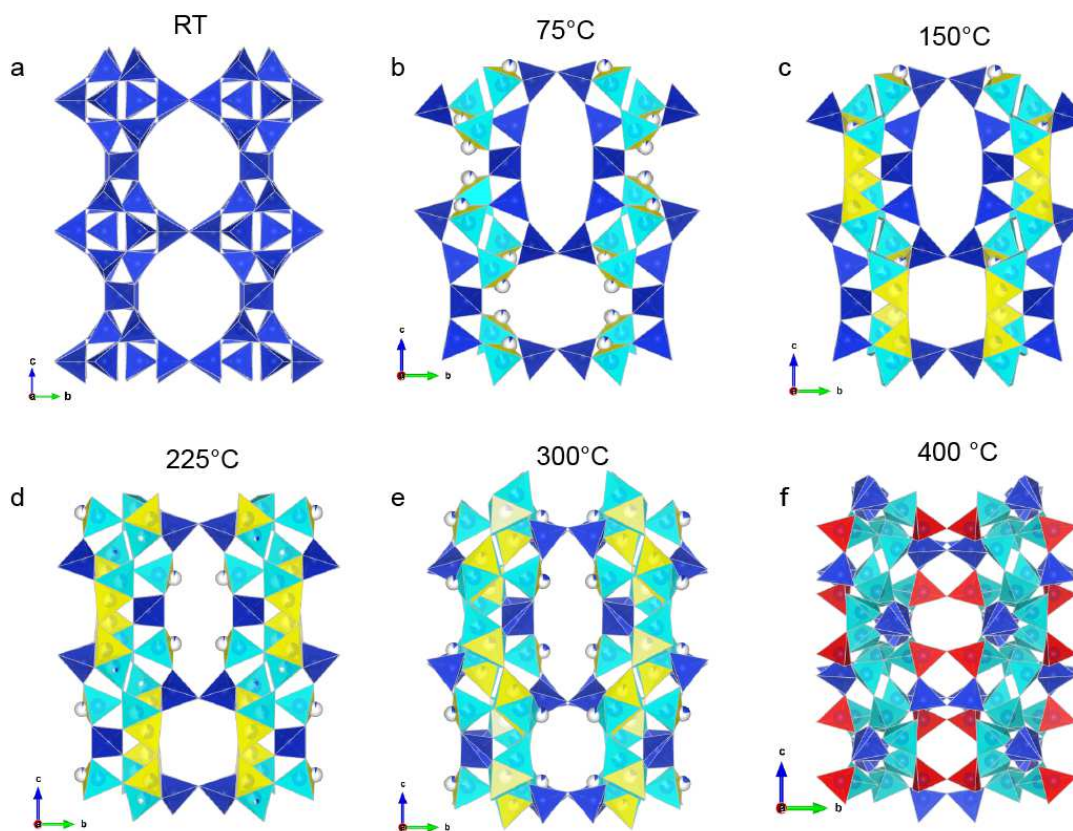


Figure 7 Polyhedral representation of the crystal structure of Ag-STI at RT (a), 75 (b), 150 (c), 225 (d), 300 (e), and 400 °C (f). (Si,Al)O₄ tetrahedra are depicted in blue. The tetrahedra involved in the T-O-T rupture are shown in cyan whereas the new T sites originating as a consequence of the T migration are yellow. Partially colored spheres represent low occupied T sites. Red tetrahedra in the structure at 400°C (f) correspond to those flipped inside the channels parallel to [100].

onset of the dehydration was observed at 50°C, indicated by the drop of the unit-cell volume from 4392.85(14) to 4093.0(2) Å³ corresponding to ca 7% of that measured at room temperature (Fig. 6). The main structural changes of the Ag-STI framework, as a function of temperature, are shown in Fig. 7a-f: the polyhedral representation was chosen to better visualize the T-O-T breaking processes.

At 50°C, the space group changed from $F2/m$ to $A2/m$ and the ten-membered ring channels parallel to [100] narrowed and became more elliptical. Moreover, the occurrence of a new low occupied site T4D ($Occ. = 0.029(4)$) close to the tetrahedral site T4 indicated that the rupture of the T-O-T connections started already at this temperature. At 75°C the new sites T1MD, T2D, and T4MD appeared at 1.10(3), 1.171(17), and 1.12(2) Å from T1M, T2 and T4M respectively (Table S1, Fig. 7b). The T-O-T bonds involved in this breaking process were the same (T4-O5-T2 and T1M-O3-T4M) as in Na-stellerite³³, though the process started at lower temperature in Ag-STI. Upon heating, the percentage of broken bonds increased, and at 150°C the new connections T1MD-OD2-T4MD and T4D-OD1-T2D (Table S2), observed in Na-stellerite only at 275°C³³, formed (Fig. 7c). With the increase of temperature, the unit-cell volume further decreased, and at 225°C partial migration (not observed in Na-stellerite) of the T1 and T2M sites toward new positions was also observed (Table S3, Fig. 7d). At 275°C the occupancies of the new T sites converged to ca. 57% (T2D and T4D), 45% (T1MD and T4MD) and 7% (T1D and T2MD). At this temperature the structure was assumed to be anhydrous.

Between 300 and 400°C structures solution pointed to the orthorhombic space group $A2_1ma$. The latter corresponds to the space group of the D phase obtained at 400°C for barrerite^{30,34} and *ex-situ* at 525°C for Na-stellerite³³. Although the space group was the same, the Ag-STI reached the D phase configuration only at 400°C (Table S4, Fig. 7f); between 300 and 350°C the structure adopted an intermediate topology between the B and the D phase. This new topology, called D', was observed here for the first time. It has the space group $A2_1ma$, like the D phase, but it is still characterized by the system of statistically occupied face-sharing tetrahedra (Table 5, Fig. 7e).

For the sake of clarity, the correspondence between the tetrahedral sites in the orthorhombic and monoclinic space group between B, D' and D phases is reported in Table S5. The three

configurations, the B, D' and D phases are shown in Fig. 8. In the B phase, the original T sites (in cyan) statistically “moved” toward the new positions (reported in yellow). A corresponding process is not maintained in the D' phase, where some of the T sites migrated into the opposite direction: part of them remained at their original positions whereas others completely moved to new ones. For example, in the B phase 45% of the T sites, originally at T4M and T1M, occupy the new tetrahedral positions at T4MD and T1MD, respectively (Fig. 8a). In the D' phase the occupancies of the new

Table 5 Atom coordinates, equivalent displacement parameters, and occupancy of D' phase of Ag-STI at 300°C.

Site	Scattering factor	x	y	Z	U ^{ani}	Occ.
Framework						
T1	Si	0.4466(5)	0.6818(5)	0.9578(4)	0.0533(18)	0.789(11)*
T1D	Si	0.427(3)	0.720(2)	0.894(2)	0.068(9)	0.211(11)*
T1A	Si	0.6237(5)	0.5895(4)	0.1961(4)	0.0568(17)	1
T2	Si	0.5834(5)	0.8203(3)	0.0091(5)	0.0569(15)	1
T2A	Si	0.5410(5)	0.5897(3)	0.8046(4)	0.0527(16)	1
T3	Si	0.917(3)	0.594(3)	0.873(3)	0.039(9)	0.106(6)
T3N	Si	0.9337(6)	0.6674(6)	0.8527(6)	0.063(2)	0.789(11)*
T3ND	Si	0.935(2)	0.6940(17)	0.7842(19)	0.012(6)	0.106(6)
T3A	Si	0.4410(5)	0.1454(5)	0.1422(5)	0.0479(18)	0.789(11)*
T3AD	Si	0.428(4)	0.089(3)	0.132(3)	0.090(12)	0.211(11)*
T4	Si	0.7324(6)	0.6939(5)	0.7881(5)	0.060(2)	0.865(18)**
T4D	Si	0.7267(18)	0.6720(15)	0.8554(16)	0.019(9)	0.135(18)*
T4A	Si	0.7155(4)	0.8582(4)	0.8656(4)	0.0534(16)	1
T5	Si	0.7375(6)	0.7763(5)	0.6157(5)	0.0545(18)	0.789(11)*
T5D	Si	0.222(2)	0.6894(19)	0.9619(17)	0.0545(18)	0.211(11)*
O2	O	0.6415(14)	0.8767(10)	-0.0578(13)	0.075(5)	1
O3	O	0.569(3)	0.5	0.822(3)	0.111(11)	1
O4	O	0.771(2)	0.7284(16)	0.6974(15)	0.087(7)	0.865(18)**
O5	O	0.7052(15)	0.7681(12)	0.8436(12)	0.073(5)	1
O6	O	0.5125(15)	0.7659(12)	-0.0403(13)	0.075(5)	1
O7	O	0.617(2)	0.5	0.164(2)	0.083(7)	1
O8	O	0.6818(16)	0.9104(12)	0.7866(13)	0.078(5)	1
O9	O	0.670(4)	0.767(3)	0.048(4)	0.089(16)	0.5
O9A	O	0.657(4)	0.718(3)	0.574(4)	0.093(16)	0.5

O11	O	0.6418(15)	0.6372(13)	0.7804(13)	0.077(5)	1
O12	O	0.688(2)	0.6374(17)	0.1345(17)	0.109(8)	1
O13	O	0.495(2)	0.6222(16)	0.8907(16)	0.102(7)	1
O14	O	0.4613(15)	0.5990(12)	0.7338(13)	0.078(5)	1
O15	O	0.8289(16)	0.8828(10)	0.8877(11)	0.076(4)	1
O16	O	0.334(2)	0.7051(14)	0.9386(16)	0.106(6)	1
O17	O	0.4520(17)	0.6397(14)	1.0519(15)	0.070(6)	0.789(11)*
O18	O	0.5122(18)	0.6252(17)	0.2033(16)	0.099(7)	1
O19	O	0.8242(18)	0.6437(11)	0.8238(12)	0.080(4)	1
O20	O	0.5188(13)	0.8799(11)	0.0678(12)	0.070(5)	1
OD1	O	1.008(3)	0.726(3)	0.691(3)	0.019(9)	0.211(11)*
OD4	O	0.710(5)	0.657(4)	-0.046(4)	0.022(16)	0.135(18)**
OD3	O	0.9488(15)	0.7582(12)	0.8459(13)	0.078(5)	1

Extraframework

Ag1	Ag	0.8294(7)	0.5	0.275(2)	0.043(4)	0.35(4)
Ag1B	Ag	0.838(3)	0.5	0.307(5)	0.071(13)	0.11(3)
Ag1A	Ag	0.8279(10)	0.5	0.246(2)	0.058(5)	0.27(4)
Ag1C	Ag	0.846(10)	0.5	0.175(8)	0.08(6)	0.025(16)
Ag2	Ag	0.553(3)	0	0.039(2)	0.045(14)	0.084(19)
Ag2A	Ag	0.794(5)	0.5	0.108(5)	0.12	0.072(13)
Ag2B	Ag	0.622(2)	1	-0.0204(17)	0.111(12)	0.26(3)
Ag2C	Ag	0.604(2)	1	0.0322(18)	0.061(12)	0.13(2)
Ag2D	Ag	0.512(6)	1	-0.007(4)	0.16(3)	0.14(4)
Ag2E	Ag	0.573(2)	1	-0.068(2)	0.147(15)	0.26(3)
Ag2F	Ag	0.5711(16)	1	-0.0071(15)	0.053(9)	0.17(3)
Ag3	Ag	0.761(8)	0.5	0.772(11)	0.12	0.06(2)
Ag3A	Ag	0.773(2)	0.5	0.812(3)	0.076(15)	0.13(3)
Ag4	Ag	0.998(3)	0.5	-0.0218(17)	0.102(14)	0.18(3)
Ag4A	Ag	1.048(3)	0.5	-0.0064(18)	0.112(15)	0.24(5)
Ag4B	Ag	1.073(4)	0.459(4)	-0.015(3)	0.07(2)	0.044(14)
AgO1	Ag	0.9691(14)	0.6980(13)	0.6754(9)	0.112(7)	0.28(2)
AgO2	Ag	0.848(6)	0.5	0.806(5)	0.15	0.099(15)
AgO3	Ag	0.9405(13)	0.6627(12)	0.6597(10)	0.093(7)	0.203(19)

* $Occ.T1 = Occ.T3A = Occ.T5 = Occ.O17 = 1 - Occ.T1D = 1 - Occ.T3AD = 1 - Occ.T5D = Occ.T3N = 1 - Occ.OD1$

* $Occ.T3N = 1 - Occ.(T3 + T3ND)$

** $Occ.T4 = Occ. O4 = 1 - Occ. T4D = 1 - Occ. OD4$

positions (T3N and T1 in D' are equivalent to T4MD and T1MD in B) increase to 78%, indicating that the migration process continued (Fig. 8b). In a similar way, in the B structure, 58% of the original T4 and T2 sites moved to T4D and T2D (Fig. 8a): in contrast, the occupancies of the

corresponding T sites in the D' structure (T4 and T5 in D' are equivalent to T4 and T2 in B) decreased to approximately 20% (Fig. 8b), indicating that in this case the migration process inverted.

Thus, the T sites in the D' phase are approaching the final configuration that they will adopt in the D structure. In addition, in the D topology, part of the tetrahedra (displayed in red in Fig. 7f and Fig. 8c) flipped within the ten-membered ring channel, leading to the occlusion of the pores along [001] and [100] (Fig. 7f). Such changes are accompanied by further contraction of the unit-cell volume, which at 400°C reached 3644.4(4) Å³.

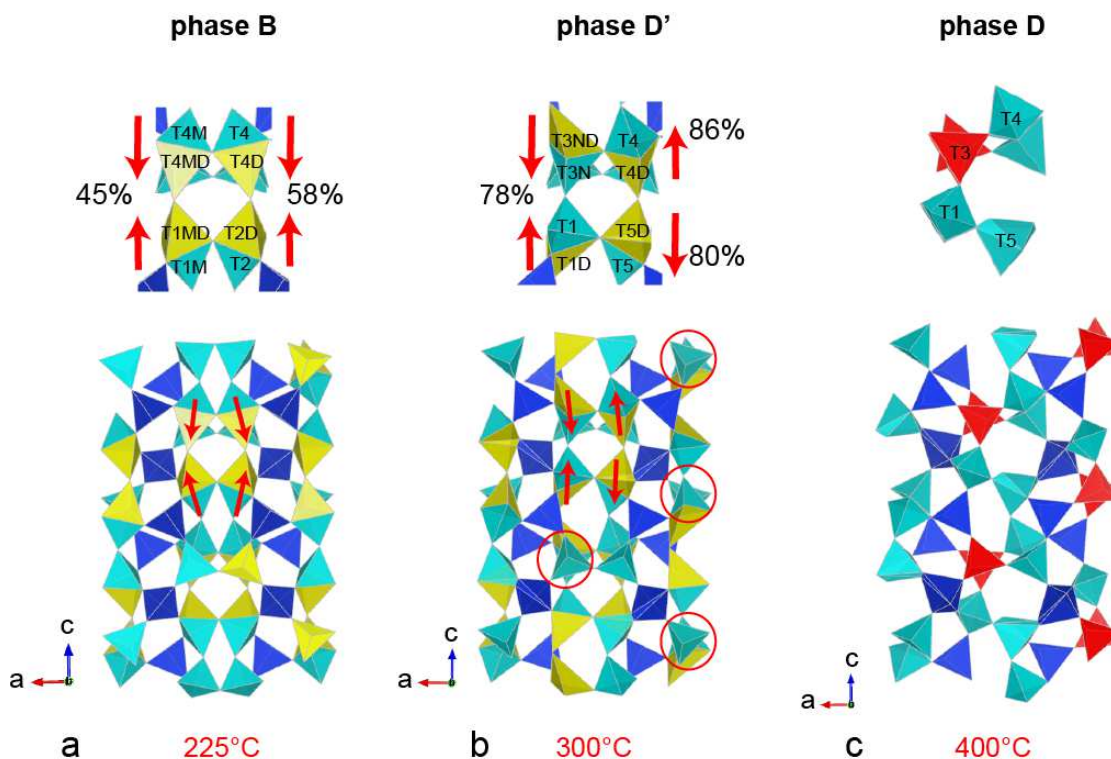


Figure 8 Polyhedral representation of Ag-STI phase B (a), phase D' (b), and phase D (c) projected along [010]. Color code as in Fig. 7. The red arrows indicate the direction of migration of T sites. The percentages refer to the relative occupancies of T sites involved in the breaking process. The red circle highlighted the tetrahedra in phase D' that will flip and occlude the channels in phase D (red tetrahedra).

The disordered arrangement of Ag^+ ions was observed in the whole temperature range. In the anhydrous structures, and in particular from 300 to 400°C, the Ag^+ ions were at average bonding distances to framework oxygen between 2.3 and 2.6 Å.

Evolution of the local Ag coordination upon heating. The EXAFS spectra show a systematic evolution from 25° to 650° C, most easily seen in the FTM as an increase of the intensity of the shorter Ag-O peak and a decrease of the longer Ag-O peak (Fig. 9). All spectra can be nicely reproduced with only two principal components (Fig. 9), further confirmed by a Malinowski indicator minimum for principal component 2, suggesting that Ag adopts mainly two different local environments across the temperature series. Factor loadings after VARIMAX rotation with the ITFA program package show that the spectra measured at 25 and 650°C represent the two extremes most purely. Assuming that both are the structural end-member components by setting their fractions to 100% of component 1 and 2, respectively, we derived the fractions at the intermediate temperatures by iterative transformation target test using ITFA (Table 6).

On the basis of XRD results, we see two end-members with ordered framework topology: 1) the hydrated A phase and 2) the dehydrated D phase. The B and the D' phases (discussed in XRD results) represent intermediate structural configurations. The percentage of the two components retrieved from ITFA can be compared with the percentage of the T-O-T bridges, calculated from XRD data, which break upon heating. It should be stressed that the 'percentage of broken bridges' describes two structural configurations (e.g. A and B) that are statistically present at a given temperature. Thus, the concentration of a given phase at a given temperature is represented by the refined occupancies of the tetrahedral sites detected by XRD. In Table 6 we compare these values with the percentage of the two components calculated by ITFA of EXAFS spectra. From 25 to 275°C, we considered the occupancies of T1M and T1MD sites as those representing the

component 1 and 2, respectively. The T4D and T4 occupancies refined at 350 and 400°C were chosen to represent the two components at 350 and 425°C. The values extrapolated from EXAFS match those obtained by SC-XRD. According to these results, the dehydration process can be described by a gradual transition from one topology to another without abrupt structural changes. The structural parameters (Table 4) of the two components correspond to those obtained by fitting the EXAFS spectra at 25 and 650°C. A four-shell model was applied to reproduce the spectrum at 650°C: two Ag-O (split-oxygen), one Ag-Si, and one Ag-Ag. Compared to the structural parameters obtained at 25°C, the average oxygen coordination of Ag⁺ decreased from 4.3 to 2.9. Simultaneously, the Ag-Ag distance increased from 2.92 to 3.31 Å, and the Ag-Si distance decreased from 3.76 to 3.44 Å.

Table 6 Relative concentration of the two components used to reconstruct the spectra by ITFA. Refined occupancies of tetrahedral sites obtained by XRD associated with end-member components.

T (°C)	EXAFS			XRD	
	Component 1 (phase A)	Component 2 (phase D)	sum	Component 1 (phase A)	Component 2 (phase D)
25	1.00	0.00	1.00	1.0	0.0
75	1.00	0.20	1.20	0.90	0.10
175	0.66	0.50	1.17	0.70	0.30
275	0.41	0.68	1.09	0.43	0.57
350	0.24	0.87	1.11	0.10	0.90
425	0.21	0.93	1.14	0*	1*
550	0.00	1.00	1.00	-	-
650	0.00	1.00	1.00	-	-

*corresponding to refined occupancies obtained at 400°C

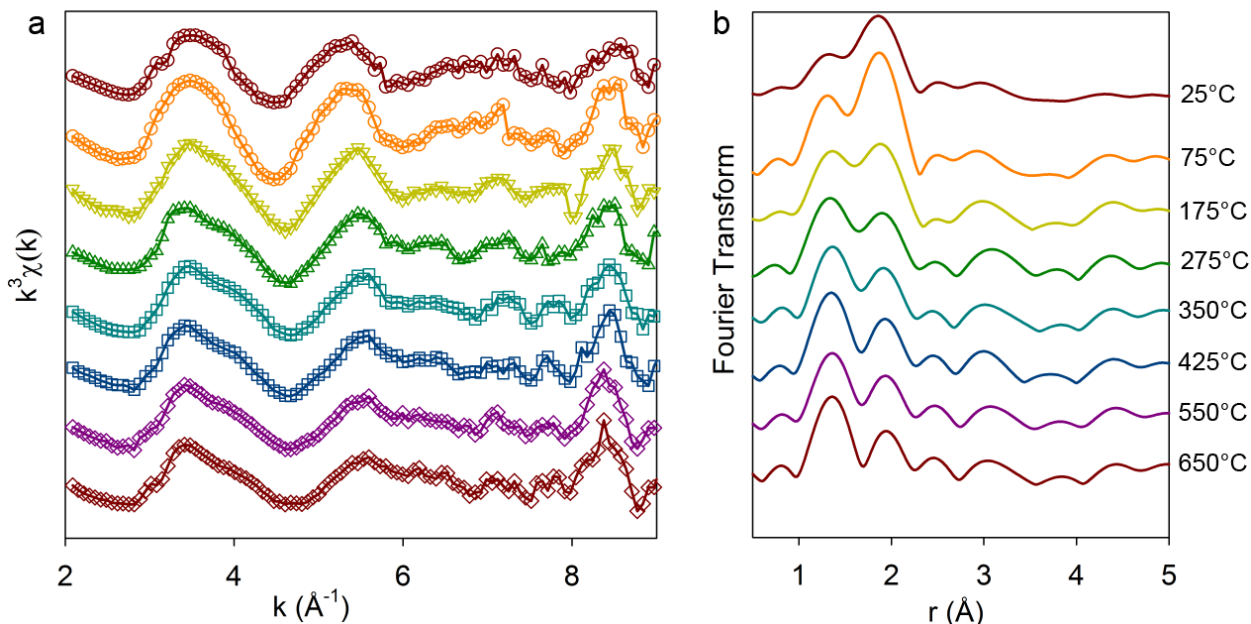


Figure 9 (a) $k^3\chi(k)$ weighted EXAFS spectra experimental (solid line) and reconstruction by two components (symbol), and (b) corresponding Fourier-transform calculated by ITFA.

The decrease of the CN of the Ag-O shell was expected as a consequence of dehydration upon heating. To reach a favorable coordination after the loss of H_2O , Ag^+ ions bond to the oxygen of the framework. This could also explain the increase of the Ag-Ag and decrease of Ag-Si distances. Hence the Ag^+ ions, initially located also in the center of the cages, migrate closer to the channel walls. The structural parameters obtained from the fitting of the EXAFS data in the whole temperature range (25-650°C) are provided as supporting information in Table S6.

3.3 Do Ag-clusters form? The formation of small silver clusters, neutral or charged, was demonstrated to occur in a variety of zeolites, natural and synthetic. The clustering of silver atoms in Ag-exchanged zeolites was reported after treatment at high temperature^{58,59,60,61} and /or in reducing atmospheres^{58,62}.

Due to the strong disorder of Ag atoms, the analysis of X-ray does not unambiguously allow to confirm or rule out potential formation of metallic silver clusters (e.g. Ag₂, Ag₃, Ag₄, etc.) at high temperature. In the structure obtained at 400°C (Ag-STI phase D) eight main Ag sites (Ag1, Ag8) were located. If we exclude the short Ag-Ag distances (between 0.50 and 2.00 Å), too short to be either due to Ag⁺-Ag⁺ or Ag⁺-Ag⁰ interactions⁶², the only possibly meaningful Ag-Ag contacts are Ag5-Ag2 = 2.85(13) Å, Ag6-Ag3D = 2.81(6) Å, and Ag6-Ag2A = 2.90(17) Å. In principle, these distances could represent Ag⁰-Ag⁰ interactions⁶²; however, both Ag5 and Ag6 sites are very low occupied (0.031(10) and 0.019(14) respectively) and these values are affected by high standard deviations. The EXAFS data obtained at RT indicated a Ag-Ag shell with CN = 0.2 and R = 2.92 Å (Table 4). The fitting of the spectrum measured at 650°C, showed that the Ag-Ag distance increased to 3.31 Å. This value is too high to be interpreted as a Ag⁰-Ag⁰ interaction⁶² but similar to Ag⁺-Ag⁰ distances found in Ag-A (3.31 Å)⁶³ and Ag-Y (3.24 Å)⁶⁴ zeolites. Nevertheless, in our case, the presence of Ag⁰ atoms is not supported by Ag-O distances (and by XANES spectra), which are considerably shorter (2.14 and 2.37 Å, and between 2.3-2.6 Å as retrieved by EXAFS and XRD, respectively) compared to typical Ag⁰-O distances (= 2.78 Å)⁶².

As a further consideration, the formation of Ag clusters is generally associated with change in color of the sample^{17,59,65,66,67}. Experiments^{63,65,68} and quantum-chemical calculations⁶⁹ indicated that color change corresponds to charge transfer from framework oxygens to Ag cations. Thus, dehydration and the associated increasing number of Ag clusters is responsible for the yellow color of some Ag-exchanged zeolites. In contrast, “shortest Ag-O bonds and darkest colors occur when little or no water is retained and little or no Ag⁺ has been reduced”⁵⁹. In this study, the powder used in EXAFS experiments turned grey but not yellow, whereas the single-crystal was colorless at the beginning and grey at the end of the HT-XRD experiments. Thus, although the formation of

silver clusters ($\text{Ag}^+\text{-Ag}^+$) cannot be completely excluded, the reduction of Ag^+ to Ag^0 is highly unlikely.

4. CONCLUSIONS

The incorporation of Ag^+ ions into the stellerite structure causes a monoclinic distortion ($F2/m$) of the orthorhombic symmetry ($Fmmm$), characteristic of the natural form (e.g. Ca rich member). The same distortion, though less severe, was also observed in the Na-exchanged form of stellerite³³. The disordered arrangement of the Ag^+ ions within the cages is significantly more pronounced than that of Na in the Na-exchanged form. The dehydration behavior is also affected by the EF cation substitution: the structural transformations upon heating are shifted toward lower temperature than those reported for Na-stellerite. Furthermore, the Ag-STI transforms between 300 and 400°C to a new topology (phase D') that was never observed before.

The effects of the incorporation of various EF cations into the same zeolite framework-type and the response of the framework itself, are not only dependent on the atomic radius and charge of the exchanged cation. The different electronic configuration and specifically, the d orbitals of Ag^+ , compared to the p orbitals of Na^+ , results in a different interaction with the framework and H_2O oxygen. In a study on the adsorptive properties of various cationic forms of zeolite X⁷⁰ Habgood (1964) already concluded that silver ions have “much stronger polarizing power” than sodium and the d orbitals provide “more intense directional properties”. In our case, this may justify the strong disorder of the Ag^+ ions within the cages and, as a consequence, the stronger monoclinic distortion of the aluminosilicate framework.

Our findings demonstrated that starting from a natural material it is possible to produce new phases. In particular, different cations stabilize different structures with different microporous

properties. The stability and the properties of the new-obtained material can significantly change with respect to the pristine zeolite: this is a crucial point to consider when zeolites are modified by the incorporation of transition metals.

Supporting Information. The following material is provided in the Supporting Information file. Paragraph 1 provides additional details on the strategy used to refine the SC-XRD data. Figure S1 shows the SEM-EDX spectra of single crystal (used for SC-XRD experiments) and powder (used for EXAFS measurements) Ag-STI. Figure S2 and S3 report the wavelet plot and the XANES spectra, respectively, of Ag-STI at 25°C and 650°C. Figure S4 shows the SEM picture of the small particles found in the powder used for EXAFS measurements. TableS1, S2, S3, S4 contain the atom coordinates, equivalent displacement parameters and occupancy of Ag-STI structures at 75, 150, 225, and 400°C respectively. Table S5 reports the correspondence between the tetrahedral sites of B, D', and D phases. Structural parameters determined from EXAFS data from 25 to 650°C are listed in Table S6.

AUTHOR INFORMATION

Corresponding Author

*Georgia Cametti eMail: georgia.cametti@krist.unibe.ch.

Tel.: +41 31 631 5248

ORCID: Georgia Cametti: 0000-0002-3186-3074

Author Contributions

G. C: conceived the research, performed the experiments, analyzed the data and wrote the manuscript. A. S. analyzed the EXAFS data, M. G. performed the EXAFS experiments and S. C. set up the MD simulations. The manuscript was written through contributions of all authors. All authors have given approval to the final version of the manuscript.

Funding Sources

This study benefits from funding awarded to G. C. by the Swiss National Science Foundation (SNF): Ambizione Grant Nr. PZOO2_173997.

ACKNOWLEDGMENTS

The authors acknowledge access to the Swiss National Supercomputing Centre (CSCS) and UBELIX HPC cluster at university of Bern. We are thankful to Thomas Armbruster for his comments and suggestions and to Germán Castro of the Spanish CRG Beamline at ESRF in Grenoble for his support and help during the EXAFS experiments.

REFERENCES

- (1) Gottardi, G.; Galli, E. *Natural Zeolites*; Springer-Verlag Berlin Heidelberg, New York Tokyo, 1985.
- (2) Bish, D. L.; Ming, D. W. *Natural Zeolites: Occurrences, Properties and Applications*. Reviews in Mineralogy and Geochemistry, 45. Mineralogical Society of America and Geochemical Society, Washington DC, 2001.
- (3) Ackley, M. W.; Rege, S. U.; Saxena, H. Application of natural zeolites in the purification and separation of gases. *Micropor. Mesopor. Mat.* **2003**, 61, 25-42.
- (4) Colella, C. Environmental applications of natural zeolitic materials based on their ion-exchange properties, in: P. Misaelides, F. Macasek, T.J. Pinnavaia, C. Colella (Eds.), *Application of Natural Microporous Materials in Environmental technology*, Kluwer, NATO Science Series vol. E362 (Applied Sciences), Dordrecht, 1999.
- (5) Babel, S.; Kurniawan, T. A. Low-cost adsorbents for heavy metals uptake from contaminated water: a review. *J. Hazard. Mater.* **2003**, 97, 219-243.
- (6) Borai, E. H.; Harjula, R.; Malinen, R.; Paajanen, A. (2009) Efficient removal of cesium from low-level radioactive liquid waste using natural and impregnated zeolites minerals. *Journal of Hazardous Materials* 172, 416-422. Misaelides, P. Application of natural zeolites in environmental remediation: A short review. *Micropor. Mesopor. Mat.* **2011**, 144, 15-18.
- (7) Wang, S.; Peng, Y. Natural zeolites as effective adsorbents in water and wastewater treatment. *Chem. Eng. J.* **2010**, 156, 11-24.
- (8) Armenta, G. A.; Ramirez, G. H.; Loyola, E. F.; Castaneda, A. U.; Gonzales, R. S.; Munoz, C. T.; Lopez, A. J.; Castellon, E. R. Adsorption kinetics of CO₂, O₂, N₂, CH₄ in Cation-Exchanged Clinoptilolite. *J. Phys. Chem. B* **2001**, 105, 1313-1319.
- (9) Lee, H. K.; Shim, M. J.; Lee, J. S.; Kim, S.W. Characteristics of CO gas adsorption on modified natural zeolite. *Mater. Chem. Phys.* **1996**, 44, 79-84.

- (10) Chao, C. C.; Rastelli, H. US Patent 5,116,793, **1992**.
- (11) Kasture, M. W.; Joshi, P. N.; Sorti, H. S.; Joshi, V. V.; Choudari, A. L.; Shiralkar, V. P. Sorption Properties of the Natural, K and partially Deammoniated (H/NH₄) forms of clinoptilolite. *Adsorp. Sci. Technol.* **1998**, 16, 135-151.
- (12) Ogawa, H.; Ito, Y.; Nakano, M.; Itabashi, K. US Patent 6,309,616, **2001**.
- (13) Knaebel, K. S.; Kandybin, A. US Patent 5,226,933, **1993**.
- (14) Coe, C. G.; Gaffney, T. R.; Srinivasan, R.S. US Patent 4,925,460, **1990**.
- (15) Boniface, H. A.; Ruthven, D. M. Selectivity of some zeolites for adsorption of atmospheric gases. *Gas Sep. Purif.* **1993**, 7, 183-184.
- (16) Zukal, A.; Pulido, A.; Gil, B.; Nachtigall P.; Bludský, O.; Rubeš, M.; Čejka J. Experimental and theoretical determination of adsorption heats of CO₂ over alkali metal exchanged ferrierites with different Si/Al ratio. *Phys. Chem. Chem. Phys.* **2010**, 12, 6413-6422.
- (17) Hutson, N. D.; Reisner, B. A.; Yang, R. T.; Toby, B. H. Silver ion-exchanged zeolites Y, X, and low-silica X: Observations of thermally induced cation/cluster migration and the resulting effects on the equilibrium adsorption of Nitrogen. *Chem. Mater.* **2000**, 12, 3020-3031.
- (18) Chen, X.; Benxian, S.; Sun, H.; Zhan, G. Ion-exchange modified zeolites X for selective adsorption desulfurization from Claus tail gas: Experimental and computational investigations. *Micropor. Mesopor. Mat.* **2018**, 227-236.
- (19) Coutino-Gonzales, E.; Baekelant, W.; Grandjean, D.; Roeffaers, M. B. J.; Fron, E.; Aghakhani, M. S.; Bovet, N.; Van der Auweraer, M.; Lievens, P.; Vosch, T.; Sels, B.; Hofkens, J. Thermally activated LTA(Li)-Ag zeolites with water-responsive photoluminescence properties. *J. Mater. Chem. C* **2015**, 3, 11857-11867.
- (20) Ferreira, L.; Fonseca, A. M.; Botelho, G.; Aguiar C. A.; Neres, I. C. Antimicrobial activity of faujasite zeolites doped with silver. *Micropor. Mesopor. Mat.* **2012**, 160, 126-132.
- (21) Milenkovic, J.; Hrenovic, J.; Matijasevic, D.; Niksic, M.; Rajic, N. Bactericidal activity of Cu-, Zn-, Ag-containing zeolites toward Escherichia coli isolates. *Environ. Sci. Pollut. Res.* **2017**, 24, 20273-20281.
- (22) Baerlocher, C.; Meier, W. M.; Olson, D. H. Atlas of Zeolite Framework Types, Structure Commission of the IZA, fifth ed., Elsevier, **2001**.
- (23) Galli, E.; Alberti, A. The crystal structure of stellerite. *B. Soc. Fr. Mineral. Cr.* **1975**, 98, 11-18.
- (24) Galli, E. Refinement of the crystal structure of stilbite. *Acta Crystallogr. B* **1971**, 833-841.
- (25) Galli, E.; Alberti, A. The crystal structure of barrerite. *B. Soc. Fr. Mineral. Cr.* **1975**, 98, 331-340.
- (26) Ghobarkar, H.; Schäfer, O. Synthesis of stilbite by the hydrothermal method. *J. Phys. D: Appl. Phys.* **1998**, 31, 3172-3176.
- (27) Hong, S. B.; Lear, E. G.; Wright, P. A.; Zhou, W.; Cox, P. A.; Shin, C. H.; Park, J. H.; Nam, I.S. Synthesis, structure solution, characterization, and catalytic properties of TNU-10: A high-silica zeolite with the STI topology. *J. Am. Chem. Soc.* **2004**, 126, 5817-5826.
- (28) Alberti, A.; Rinaldi, R.; Vezzalini, G.; Dynamics of dehydration in stilbite-type structures; Stellerite phase B. *Phys. Chem. Miner.* **1978**, 2, 365-375.
- (29) Cruciani, G.; Artioli, G.; Gualtieri, A.; Ståhl, K.; Hanson, J. C. Dehydration dynamics of stilbite using synchrotron X-ray powder diffraction. *Am. Mineral.* **1997**, 82, 729-739.

- (30) Ori, S.; Mazzucato, E.; Vezzalini, G. Dehydration dynamics of barrerite: An in situ synchrotron XRPD study. *Am.Mineral.* **2009**, 94, 64-73.
- (31) Arletti, R.; Mazzucato, E.; Vezzalini, G. Influence of dehydration kinetics on T-O-T bridge breaking in zeolites with framework type STI: The case of stellerite. *Am. Mineral.* **2006**, 91, 628-634.
- (32) Cametti, G.; Armbruster, T.; Nagashima, M.; Thermal stability of barrerite and Na-exchanged barrerite: An in situ single crystal X-ray diffraction study under dry conditions. *Micropor. Mesopor. Mat.* **2016**, 236, 71-78.
- (33) Cametti, G.; Fisch, M.; Armbruster, T. Thermal behavior of stilbite and stellerite revisited and dehydration of their Na-exchanged forms: Considerations on the memory effect of the STI framework type. *Micropor. Mesopor. Mat.* **2017**, 253, 239-250.
- (34) Sacerdoti, M. The crystal structure of zeolite barrerite dehydrated in air at 400-450°C. *Micropor. Mesopor. Mat.* **2007**, 102, 299-303.
- (35) Armbruster, T., Kohler, T., Meisel, T.; Nägler, T. F.; Götzinger, M. A.; Stadler, H. A. The zeolite, fluorite, quartz assemblage of the fissures at Gibelsbach, Fiesch (Valais, Switzerland): crystal chemistry, REE patterns and genetic speculations. *Mineral. Petrogr. Mitt.* **1996**, 76, 131-146.
- (36) Bruker AXS, APEX2 v2012.10-0.
- (37) Sheldrick, G. M. A short history of SHELX. *Acta Crystallogr. A* **2008**, 64, 112-122.
- (38) Quartieri, S.; Vezzalini, G.; Crystal chemistry of stilbites: structure refinements of one normal and four chemically anomalous samples. *Zeolites* **1987**, 7, 163-170.
- (39) Sheldrick, G. M. Crystal structure refinement with SHELXL. *Acta Crystallogr. C* **2015**, 71, 3-8.
- (40) Momma, K.; Izumi, F. VESTA 3 for three-dimensional visualization of crystal, volumetric and morphology data. *J. Appl. Crystallogr.* **2011**, 44, 1272-1276.
- (41) Bussi, G.; Donadio, D.; Parrinello, M. Canonical sampling through velocity rescaling. *J. Chem. Phys.* **2007**, 126, 014101.
- (42) www.cp2k.org
- (43) VandeVondele, J.; Krack, M.; Mohamed, F.; Parrinello, M.; Chassaing, T.; Hutter, J. Quickstep: Fast and accurate density functional calculations using a mixed Gaussian and plane waves approach. *Comput. Phys. Comm.* **2005**, 167, 103-128.
- (44) Perdew, J.P.; Burke, K.; Ernzerhof, M. Generalized gradient approximation made simple. *Phys. Rev. Lett.* **1996**, 77, 3865-3868.
- (45) VandeVondele, J.; Hutter, J. Gaussian basis sets for accurate calculations on molecular systems in gas and condensed phases. *J. Chem. Phys.* **2007**, 127, 114105.
- (46) Ankudinov, A. L.; Ravel, B.; Rehr, J. J.; Conradson, S. D. Real-Space Multiple-Scattering Calculation and Interpretation of X-Ray-Absorption near-Edge Structure. *Phys. Rev. B* **1998**, 58 (12), 7565-7576.
- (47) Ankudinov, A. L.; Rehr, J. J. Theory of Solid-State Contributions to the X-Ray Elastic Scattering Amplitude. *Phys. Rev. B* **2000**, 62 (4), 2437-2445.
- (48) Kéri, A.; Dahn, R.; Krack, M.; Churakov, S.V. Combined XAFS Spectroscopy and Ab Initio Study on the Characterization of Iron Incorporation by Montmorillonite. *Environ. Sci. Technol.* **2017**, 51, 10585-10594.

- (49) Kéri, A.; Dähn, R.; Krack, M.; Churakov, S. V. Characterization of structural iron in smectites — an *ab initio* based XAS study. *Environmental Science and Technology*, **2019**, in press.
- (50) Ressel, T. WinXAS: A Program for X-ray Absorption Spectroscopy Data Analysis under MS-Windows. *J. Synchrotron Radiat.* **1998**, *5*, 118-122.
- (51) Funke, H.; Scheinost, A. C.; Chukalina, M. Wavelet analysis of extended X-ray absorption fine structure data. *Phys. Rev. B* **2005**, *71*, 094110.
- (52) Abdi, H.; Williams, L. J. Principal Component Analysis. *Computation. Stat.* **2010**, *2*, 433-459.
- (53) Rossberg, A.; Reich, T.; Bernhard, G., Complexation of uranium(VI) with protocatechuic acid - application of iterative transformation factor analysis to EXAFS spectroscopy. *Anal. Bioanal. Chem.* **2003**, *376*, 631-638.
- (54) Malinowski, E. R.; Howery, D. G. Factor Analysis in Chemistry. Wiley Interscience, New York, 1980.
- (55) Yalçıntaş, E.; Scheinost, A. C.; Gaona, X.; Altmaier, M., Systematic XAS study on the reduction and uptake of Tc by magnetite and mackinawite. *Dalton Transactions* **2016**, *45*, 17874-17885.
- (56) Kabalkina, S. S.; Popova, S. V.; Serebryanaya, N. R.; Vereshchagin, L. F. A new modification of Ag₂O with a layer structure. *Dokl. Akad. Nauk SSSR* **1963**, *152*, 853-855.
- (57) Smith, V. J. Topochemistry of Zeolites and Related Materials. 1. Topology and Geometry. *Chem. Rev.* **1988**, *88*, 149-182.
- (58) Kim, Y.; Seff, K. Crystal Structure of Fully Dehydrated, Partially Ag⁺-Exchanged Zeolite 4A, Ag_{7.6}Na_{4.4}-A. Ag⁺ Ions prefer 6-Ring Sites. One Ag⁺ Ion is reduced. *J. Phys. Chem.* **1987**, *91*, 671-674.
- (59) Sun, T.; Seff, K. Silver Clusters and Chemistry in Zeolites. *Chem. Rev.* **1994**, *94*, 857-870.
- (60) Kim, S. Y.; Kim, Y.; Seff, K. Two Crystal Structures of Fully Dehydrated, Fully Ag⁺-Exchanged Zeolite X. Dehydration in Oxygen Prevents Ag⁺ Reduction. Without Oxygen, Ag_{8ⁿ⁺} (*T_d*) and *cyclo*-Ag_{4^{m+}} (near *S₄*) form. *J. Phys. Chem. B* **2003**, *107*, 6938-6945.
- (61) Aghakhani, S.; Grandjean, D.; Baekelant, W.; Coutiño-Gonzales, E.; Fron, E.; Kvasnina K.; Roeffaers M. B. J.; Hofkens, J.; Sels, B. F.; Lievens, P. Atomic scale reversible opto-structural switching of few atom luminescent silver clusters confined in LTA zeolites. *Nanoscale*, **2018**, *10*, 11467-11476.
- (62) Lee, S. H.; Kim, Y.; Seff, K. Weak Ag⁺-Ag⁺ bonding in zeolite X. Crystal structures of Ag₉₂Si₁₀₀Al₉₂O₃₈₄ hydrated and fully dehydrated in flowing oxygen. *Micropor. Mesopor. Mat.* **2000**, *41*, 49-59.
- (63) Kim, Y.; Seff, K. Structure of a Very Small Piece of Silver Metal. The Octahedral Ag₆ Molecule. Two Crystal Structures of Partially Decomposed Vacuum- Dehydrated Fully Ag⁺-Exchanged Zeolite A. *J. Am. Chem. Soc.* **1977**, *99*, 7055-7057.
- (64) Gallezot, P. The State of Catalytic Properties of Platinum and Palladium in Faujasite-type Zeolites. *Catal. Rev. Sci. Engng.* **1979**, *20*, 121-154.
- (65) Jacobs, P. A.; Uytterhoeven, J. B.; Beyer, H. K. Some Unusual Properties of Activated and Reduced AgNaA Zeolites. *J. Chem. Soc. Faraday Trans. 1* **1979**, *75*, 56-64.
- (66) Gellens, L. R.; Mortier, W. J.; Uytterhoeven. On the nature of the charged silver clusters in zeolites of type A, X, Y. *Zeolites*, **1981**, *1*, 11-18.

- (67) Gellens, L. R.; Mortier, W.J.; Schoonheydt, R. A.; Uytterhoeven, J. B. The nature of the Charged Silver Clusters in Dehydrated Zeolites of Type A. *J. Phys. Chem.* **1981**, 85, 2783-2788.
- (68) Tsutsumi, K.; Takahashi, H. The Formation of Metallic Silver in Silver-Form Zeolites. *B. Chem. Soc. Jpn.* **1972**, 45, 2332-2337.
- (69) Calzaferri, G. Forss L. An Ag-atom in the 6-6 Subunit of a Zeolite: Model Calculations. *Helv. Chim. Acta* **1986**, 69, 873-880.
- (70) Habgood, H. W. Adsorptive and gas chromatographic properties of various cationic forms of zeolite X. *Can. J. Chem.* **1964**, 42, 2340-2350.